Thermal simulation of magnetization reversals for size-distributed assemblies of core–shell exchange biased nanoparticles

J. Richy,[1,2] J.-Ph. Jay,[1] S. P. Pogossian,[1] J. Ben Youssef,[1] C. J. Sheppard,[2] A. R. E. Prinsloo,[2] D. Spenato,[1] and D. T. Dekadjevi[1, a)]

[1)]*Laboratoire de Magnétisme de Bretagne, Department of Physics, CNRS-UBO, 29285 Brest Cedex 3, France*

[2)]*Department of Physics, University of Johannesburg, PO Box 524, Auckland Park, Johannesburg 2006, South Africa*

(Dated: August 30, 2016)

A temperature dependent coherent magnetization reversal model is proposed for size-distributed assemblies of ferromagnetic nanoparticles and ferromagnetic–antiferromagnetic core–shell nanoparticles. The nanoparticles are assumed to be of uniaxial anisotropy and all aligned along their easy axis. The thermal dependence is included by considering thermal fluctuations, implemented via the Néel–Arrhenius theory. Thermal and angular dependence of magnetization reversal loops, coercive field and exchange-bias field are obtained, showing that ferromagnetic-antiferromagnetic size-distributed exchange-coupled nanoparticles exhibit temperature-dependent asymmetric magnetization reversal. Also, non-monotonic evolutions of exchange-bias and coercive fields with temperature are demonstrated. The angular dependence of coercive field with temperature exhibits a complex behavior, with the presence of an apex, whose position and amplitude are strongly temperature-dependent. The angular dependence of exchange bias with temperature exhibits complex behaviors, which depends on the AF anisotropy and exchange coupling. The resulting angular behavior demonstrates the key role of the size distribution and temperature in the magnetic response of nanoparticles.

I. INTRODUCTION

Over recent decades, magnetic nanoparticles (MNPs) have attracted a great deal of attention.[1,2] Indeed, these nanostructures exhibit different properties compared to bulk materials. This is firstly due to their reduced dimensions, secondly through the presence of interfaces, and thirdly via the inter-particle interactions.[3] Extensive research has been performed on the fundamental aspects of these properties and on technological applications such as magnetic recording and magnetic hyperthermia. The last mentioned is the field of nanomedicine treating cancer by supplying heat to tumor cells using magnetic nanoparticles and an alternating magnetic field.[4–9] One of the key points concerning the applications of MNPs is their magnetization reversal thermal dependence. In the field of magnetic hyperthermia, the heating efficiency of a particle is represented by the specific absorption rate (SAR) which is directly related to the temperature T and frequency-dependent hysteresis loop area (through hysteresis losses).[4,10] In the field of magnetic recording, a modification of the magnetization reversal over a small temperature range has key relevance for issues in applications. Firstly, such a change could be inferred by laser heating or applied current. Secondly, a device could be compromised by temperature fluctuations in a magnetic field. In addition, superparamagnetism is to be avoided in magnetic recording as it causes thermal destabilization of the recording units.[11]

Consequently, at present there is interest of understanding and determining temperature-dependent magnetization reversals for a realistic assembly of magnetic nanoparticles. In order to obtain this understanding, a particle size distribution should be incorporated in a realistic model. Indeed, previous experimental studies have shown that there will be some size distributions of the MNPs regardless of the synthesis method used.[12] This is still the case despite the fact that controlled synthesis has vastly improved in recent decades, together with advanced characterization methods. In the field of magnetic hyperthermia, the size dispersion drives the SAR.[13] The size distribution of MNPs was found to reduce the heating efficiency.[14] In the field of magnetic recording, the size distribution was found to alter the uniformity of magnetic properties and consequently compromises the accompanying technologies associated with hard disks and proposed components of patterned media.[15]

The magnetization reversals of both a size-dispersed assembly of MNPs consisting of a single ferromagnetic core, as well as that of ferromagnetic-antiferromagnetic (F–AF) core–shell nanoparticles are of interest for applications. Indeed, the F–AF core–shell nanoparticles can exhibit a magnetic interfacial exchange coupling between the core and the shell, resulting in modification of the magnetization reversal and its temperature dependence.[16] In the field of magnetic hyperthermia, the SAR of the F–AF core–shell structures were found to be nearly one order of magnitude larger than those of MNPs of the core or shell materials alone.[17,18] It is suggested that the exchange coupling at the interface can be tuned in F–AF particles with the goal of enlarging the hysteresis area for an enhanced SAR.[19] In the field of magnetic recording,[20] F–AF core–shell nanoparticles are promising for enhancing the thermal stability of magnetic bits, and overcoming the so-called *superparamagnetic limit*

[a)]david.dekadjevi@univ-brest.fr

of recording.[21,22]

Although many F and F–AF core–shell structures have been investigated experimentally and theoretically, no model describing the magnetization reversal of a size-dispersed assembly of F and F–AF core–shell nanoparticles has yet been proposed. Indeed, despite the keyrole of size distributions, previous theoretical models have solely probed the thermal behavior of single sized F and F–AF nanoparticles. It can be mentioned here that previous models based on Monte-Carlo algorithm have probed the thermal behavior either of an assembly of interacting single sized nanoparticles,[23] or of a single F or F–AF nanoparticle with complex intrinsic spin configurations.[24] Theoretical research works quantifying the temperature dependent magnetization reversal of an assembly of size dispersed magnetic nanoparticles are not reported until now. Consequently, no models were able to quantitatively predict and reproduce effects of the size distribution on the thermal behavior of the magnetization reversal whereas some of these effects are experimentally probed for many decades. It should also be noted that experimental studies on MNPs often assume that the size distribution is at the origin of some thermal dependent magnetization reversal phenomena such as the thermal dependence of critical fields, whereas interparticle interactions could also lead to similar phenomena. Providing a model including size dispersion would contribute to solve such a controversy for a given assembly of MNPs, as the contribution due to size dispersion could then be quantified.

In this manuscript, a theoretical model and study of the magnetization reversal temperature dependence for size-distributed F and F–AF core–shell particles is presented. It includes the T dependence of the reversal loops, as well as their angular dependence on the direction of the applied magnetic field (H). It should be noted here that one of the largest possible differences between experimental situation and a model is the controlled or uncontrolled misalignment between a given particle axis and the applied magnetic field. Probing the angular dependence of the reversal loops would include this into consideration.

Section II of this paper describes the theoretical model. In Sec. III, the temperature dependence of ferromagnetic-only particles is studied, including size distribution. In Sec. IV, the temperature dependence of F–AF nanoparticle magnetization reversal is studied, including an interfacial exchange coupling and a size dispersion. The results presented in Sections. III and IV reveals some thermal dependent phenomena not yet predicted, such as the presence of apexes and reduced coercive fields greater than one.

II. THERMALLY ACTIVATED EXCHANGE BIAS MODEL

In this section, a thermally-dependent exchange bias model for a single F–AF core–shell nanoparticle is described.

In the following, the F core diameter and AF shell thickness are represented by d and t_{AF} respectively, as shown in Fig. 1. The interface between F and AF volumes (V_{F} and V_{AF} respectively) is a spherical surface $S_{\mathrm{F/AF}} = \pi d^2$. All vectors and angles involved are illustrated in Fig. 2, for a two-dimensional coordinate system. The F domain has a magnetic moment $\vec{\mu}_{\mathrm{F}} = M_{\mathrm{F}} V_{\mathrm{F}} \vec{e}_{\mathrm{F}}$, with an angle θ. The AF domain has no net magnetization, but the antiparallel spins sublattice defines a direction $\vec{e}_{\mathrm{AF}}$ and can rotate with an angle α. Both F and AF domains possess an uniaxial anisotropy axis $\vec{e}_{\mathrm{ua}}$, which, for reasons of simplicity, are considered colinear. The anisotropy axis is located at an angle φ from the external field $H\vec{e}_{\mathrm{x}}$.

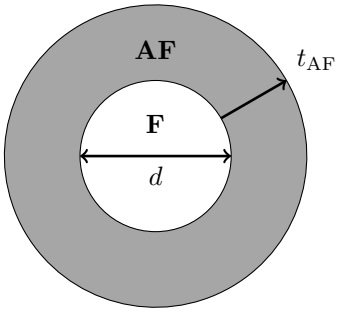

Figure 1. Geometry of the F–AF core–shell particle, with d the F core diameter and t_{AF} the AF shell thickness.

The total free energy per particle $\mathcal{F}$ is then given by:

$$\begin{aligned}\mathcal{F}(\theta,\alpha) = & -\mu_0 H \times M_{\mathrm{F}} V_{\mathrm{F}} \cos(\theta+\varphi) \\ & + K_{\mathrm{F}} V_{\mathrm{F}} \sin^2\theta \\ & + K_{\mathrm{AF}} V_{\mathrm{AF}} \sin^2\alpha \\ & - J_{\mathrm{eb}} S_{\mathrm{F-AF}} \cos(\theta-\alpha).\end{aligned} \tag{1}$$

Here, K_{F} and K_{AF} are the F and AF anisotropy constants respectively, and J_{eb} is the surface exchange energy.

Equation 1 is based on the Meiklejohn and Bean[25] (MB) model, where the magnetization reversal is coherent for both F and AF domains.

All magnetic parameters (M_{F}, K_{F}, K_{AF} and J_{eb}) are considered as temperature independent. It should be noted that previous studies[26,27] have shown that such an approximation is reasonable if no structural or magnetic transitions appear in the probed temperature range, and if the temperatures probed are not in proximity of the F and AF ordering temperatures (Curie or Néel temperature).

The physical parameters associated with the F and AF core–shell particles are listed in Tab. I. These are used for all further numerical calculations in this paper. It should be noted that F and AF physical parameters may vary largely from one system to another, especially when reducing experimental materials to the nanoscale. Even so, M_{F} and K_{F} in Tab. I correspond to reported values of Fe.[28,29] The K_{AF} constant is in good agreement with AF oxides.[30–32] The surface exchange energy J_{eb} is comparable to previous reported studies where it was found to vary largely between (3 to 840) $\mu\mathrm{J/m^2}$ for oxide based AF.[33] Finally, previous studies have reported AF shell thicknesses below a few nanometers.[22,34] Thus, these parameters are representative of actual nanoparticle systems.

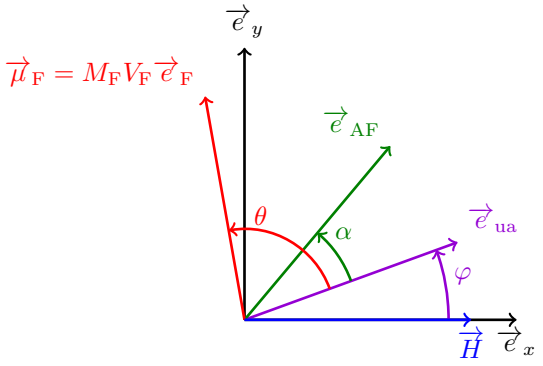

Figure 2. Diagram of the system axes, with $\vec{e}_F$, $\vec{e}_{AF}$, $\vec{e}_{ua}$ and $\vec{H}$ the F domain, AF domain, anisotropy and field axes respectively. The field direction $\vec{H}$ also defines the measurement direction of the magnetic moment.

Table I. Physical parameters used for the F-only and F–AF core–shell particles. A second set of parameters is indicated by the * exponent.

F parameters		AF parameters	
$< d >$	8 nm	t_{AF}	0.5 nm
M_F	1740 kA/m	J_{eb}	75 μJ/m^2
K_F	50 kJ/m^3	K_{AF}	200 kJ/m^3
		J^*_{eb}	10 μJ/m^2
		K^*_{AF}	100 kJ/m^3

Additionally, to achieve a compromise between accuracy and speed, the simulation resolution is 0.1° in θ for F-only particles, and 0.5° and 2° in θ and α for F–AF particles respectively. A magnetic field resolution of 0.2 mT was used for both calculations.

The analysis of $\mathcal{F}$ shows that for a given value and direction of the magnetic field (H, φ), the energy landscape is composed of one or multiple local minima, separated by saddle-points. All the particle states (α, θ) around the minimum and below the lowest surrounding saddle-point energy level define a valley region, where the F–AF directions can be trapped. Figure 3 shows an example of the free energy landscape, with four different valley regions around the red and green markers identifying local equilibria. By changing the field magnitude, the energy landscape evolves, modifying the different valley minima and also their corresponding energy barriers. In particular, at high field (i.e. above saturation), only one valley remains.

From one valley to another, when varying H, the particle equilibrium energy state has to get over the corresponding saddle-point energy barrier. Following this method, an equilibrium (α, θ couple) can be determined for each field value, and its evolution defines the magnetization reversal.

In order to introduce a thermal agitation, a transition from one valley to another is determined using the Néel-Brown relaxation theory.[35,36] Knowing the energy barrier ΔE of a local minimum of a valley, the time-dependent probability of remaining in this valley is proportional to $\exp(-t/\tau)$ with t

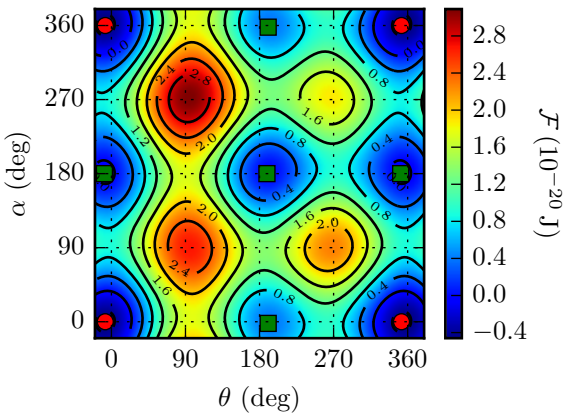

Figure 3. Free energy landscape $\mathcal{F}$, with $\mu_0 H = 15$ mT and $\varphi = 60°$. ●, stable equilibrium; ■, metastable equilibrium. ——— represent $\mathcal{F}$ iso-energy contour lines.

and τ the time and relaxation time, respectively. τ is given by Néel's law:

$$\tau = \frac{1}{f_0} \exp\left(\frac{\Delta E}{k_B T}\right), \tag{2}$$

with f_0 the attempt frequency (of the order of 10^{10} Hz),[36] k_B the Boltzmann constant, and T the temperature.

Introducing a characteristic measurement time τ_{meas}, it is commonly accepted that the transition to a new valley occurs when the relaxation time τ is below or of the same order of magnitude as τ_{meas}, which leads to

$$\Delta E < \ln(f_0 \tau_{meas}) \times k_B T. \tag{3}$$

This criterion is generally approximated to $\Delta E < 25 k_B T$.[37,38]

The method for choosing the equilibrium state considers the system state to be only in a single valley. Starting from a valley energy minimum and after a small field increment, the local minimum will have moved slightly to an energy level E_{ini}. As discussed previously, only an energy barrier lower than $25 k_B T$ compared to the reference valley can be overcome. The statistically accessible states domain $\mathcal{S}$ is defined by all the energy levels lower than $E_{ini} + 25 k_B T$ and forming a connected domain including the starting valley. This accessibility domain may contain multiple valleys and their intermediate saddle-point energy barriers.

Then the probability for the system to be in the (α, θ) state is

$$P(\alpha, \theta) = \begin{cases} \frac{1}{Z} \exp\left(-\frac{\mathcal{F}(\alpha, \theta)}{k_B T}\right), & \text{if } (\alpha, \theta) \in \mathcal{S} \\ 0, & \text{otherwise.} \end{cases} \tag{4}$$

Here Z is the partition function defined by

$$Z = \int_{\mathcal{S}} \exp\left(-\frac{\mathcal{F}(\alpha, \theta)}{k_B T}\right) \mathrm{d}\theta \, \mathrm{d}\alpha. \tag{5}$$

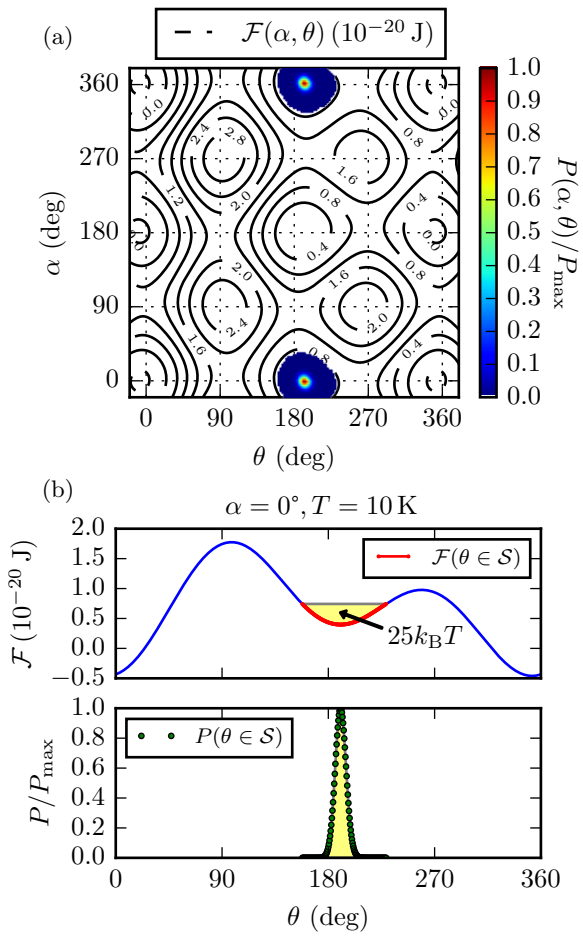

Figure 4. (a) Normalized probability function (colored area) for $T = 10\,\mathrm{K}$ with the energy landscape (black contour lines) from Fig. 3. (b) Slice for $\alpha = 0°$, with the energy function (upper) and the normalized probability (lower).
Here, the current valley corresponds to a metastable position. The $\mathcal{S}$ domain is deduced by calculating all the energy states below $25k_\mathrm{B}T$ and including the current metastable equilibrium state.

Figure 4(a) shows the example of the energy landscape from the previous figure at $T = 10\,\mathrm{K}$. The accessible domain $\mathcal{S}$ is colored in, whereas all the remaining states with zero probability are shown without color. The colored sidebar gives the normalized probability value. At this temperature, there is only one accessible local minimum, as the thermal energy is not high enough to surpass the energy barriers. Figure 4(b) corresponds to a slice for $\alpha = 0°$, with the upper part representing the energy level and the lower part showing the normalized probability.

The most probable state is then the lowest valley of $\mathcal{S}$. If this valley is different from the starting one, the equilibrium state of the system changes and jumps to this new equilibrium. Otherwise, it remains in the current valley. This process avoids the need to determining all possible saddle-points, and is repeated as many times as necessary until the selected valley remains the same.

Finally, the average magnetic moment $< \mu_\mathrm{F} >$ is deduced by integrating the projection of the magnetic moment on the field direction over all the accessible energy states $\mathcal{S}$:

$$< \mu_\mathrm{F} >= M_\mathrm{F} \int_{\mathcal{S}} P(\alpha,\theta)\cos(\theta+\varphi)\,\mathrm{d}\theta\,\mathrm{d}\alpha. \qquad (6)$$

Hence, bounds for the coercive fields, H_{c1} and H_{c2}, can be found by examining the evolution of μ_F with the external magnetic field.

It should be noted that thermal agitation may be implemented in different ways. Indeed, two different approaches have been proposed: the magnetic moment can be considered either in a one-valley state approximation as presented above,[39–41] or in a multiple-valley state approximation (with transition rates between the different valleys).[10,23,42–45] A multiple valley approximation is more difficult to process, as one needs to determine all the metastable positions and saddle-points between valleys, and resolve the time equation with all the energy levels as variable. Until now, this approach has only been used for a one-variable energy equation, whereas the free energy considered here in Eq. 1 includes two variables.

For example, the free energy landscape in Fig. 3 has 4 accessible valleys and 8 different saddle-points, which requires the resolution of 8 time-dependent differential equations with 3 independent variables as probability of presence in each valleys. Therefore, a single-equilibrium approximation with local thermal fluctuation is used in this article, allowing the F–AF particle equilibrium state (α,θ) to be in only one energy valley for a given (H,T) couple.

III. FERROMAGNETIC NANOPARTICLES

This section presents the T dependence of F-only particle magnetization reversal. Consequently, both F–AF exchange coupling J_eb and AF anisotropy constant K_AF are set to zero, the AF direction α is not considered, and the free energy function $\mathcal{F}$ only depends on H and θ.

The T dependence of H_c of a single F nanoparticle is first presented so as to examine the results of the numerical approach described in Sec. II. Following this, the T evolution of the magnetization reversal angular dependence is discussed. Indeed, this angular dependence is a key property of the magnetization reversal as it provides details about axial or/and unidirectional anisotropic properties. Thus, the temperature evolution of this angular dependence would provide key information on the axial and unidirectional anisotropic properties, so as to reveal the modifications of anisotropy configuration with temperature.[46,47]

Moreover, the presence of misalignments between anisotropy axes has been previously probed in exchange-biased systems using the magnetization reversal angular dependence. It provides key information on the ratio of anisotropy constants.[48–50] A study on exchange-biased nanoparticles will be presented in Sec. IV.

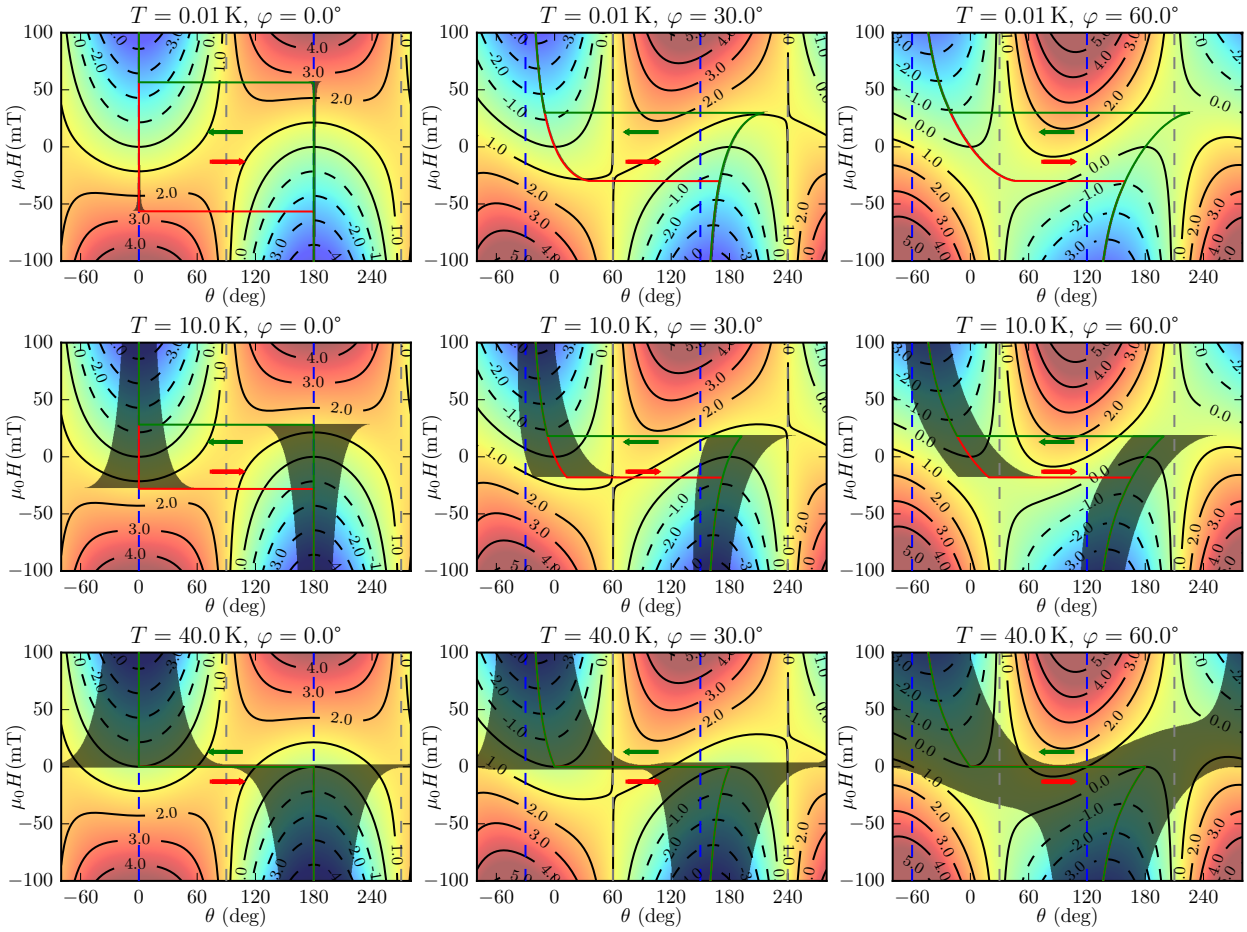

Figure 5. Evolution for a F particle of the magnetic moment direction θ with the applied field, for different field directions and at different temperatures. The ━ and ━ paths represent the decreasing and increasing branches, respectively. The colored map with iso-energy contour lines (units in 10^{-20} J) corresponds to the energy landscape $\mathcal{F}(H,\theta)$, with all the accessible directions grayed out depending on the temperature. The blue and gray dashed lines are visual guides and represent the directions parallel and perpendicular to the field direction, respectively.

A. Single F particle

The energy landscape $\mathcal{F}(H,\theta)$ is shown in Fig. 5 for an F-only particle, at different field directions and temperatures.

At $T = 0.01\,\mathrm{K}$ (in Fig. 5, first line), the magnetization reversal corresponds to the Stoner and Wohlfarth[51] (SW) reversal cycle. Indeed, μ_F follows the local valley and only experiences switching when the equilibrium disappears. For $\varphi = 0°$, i.e. with the field aligned with easy axis, the equilibrium position stays on the same axis, creating a squared hysteresis cycle. For non-zero φ, as represented in the figures shown in the second and third rows in Fig. 5, the equilibrium moves away from the field direction, reducing the measured $\mu_\mathrm{F}\cos(\theta)$ and the $\mu_0 H$ at which μ_F flips.

At $T \neq 0\,\mathrm{K}$, μ_F can reach multiple states in the local valley, reducing the energy barrier by $25k_\mathrm{B}T$. Thus, μ_F switches at a lower field strength, resulting in a decrease of H_c with T, as shown in Fig 6. As expected, the H_c decrease obtained here follows the well known[38,39] relationship:

$$H_\mathrm{c} = H_\mathrm{c}^0 \left[1 - \sqrt{25k_\mathrm{B}T/(K_\mathrm{F}V_\mathrm{F})}\right], \tag{7}$$

where H_c reaches zero when $K_\mathrm{F}V_\mathrm{F} = 25k_\mathrm{B}T$. Above this temperature defined as the blocking temperature, all the energy barriers are below $25k_\mathrm{B}T$ and the particles then have a superparamagnetic[3] behavior. μ_F can randomly flip direction under the influence of T. Thus, the time-average μ_F is zero under zero field. Figure 5 (third line) illustrates this behavior, as magnetization reversal loops corresponding to green and red paths exhibit no hysteresis at 40 K.

In the following, the angular dependence of the reduced coercive field H_c^r, defined as $H_\mathrm{c}^\mathrm{r} = H_\mathrm{c}(\varphi)/H_\mathrm{c}(\varphi = 0°)$, is studied as a function of T (see Fig. 7) for the 8 nm single particle described in Tab. I. At 0.01 K, its angular dependence reveals a butterfly-like geometry as expected from the SW model. However, the increase of T modifies the overall shape as H_c^r increases close to the hard axis. This results in a *less rounded* angular shape of H_c^r. Also, there are coercive apexes defined as local H_c maxima (arrows in Fig. 7). Their angu-

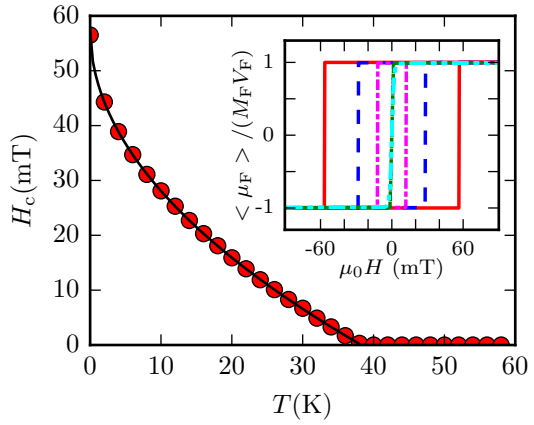

Figure 6. H_c temperature evolution (●) for $\varphi = 0°$ of a 8 nm single F particle , along with the theoretical evolution (—) using Eq. 7. The inset shows corresponding reversal cycles for $T = 0.01$ K (—), 10 K (– –), 24 K (–·–), 40 K (···) and 58 K (–··–).

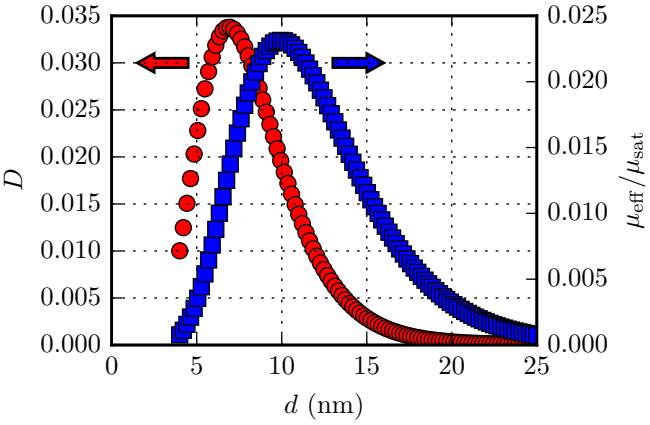

Figure 8. Lognormal particle size distribution normalized with 100 discrete diameters, (●). Effective magnetic moment per particle for each corresponding diameter, normalized with the total magnetic moment μ_{sat}, (■).

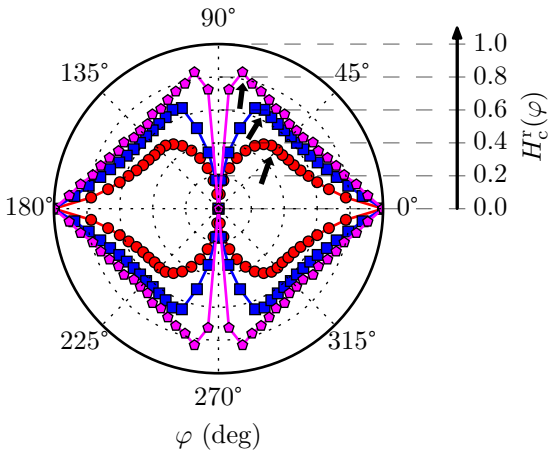

Figure 7. Azimuthal behavior of the reduced coercive field H_c^r for a single F particle at $T = 0.01$ K (●), 10 K (■) and 30 K (⊠). The arrows identify the coercive apexes positions.

lar positions evolve with T towards the hard axis, and their amplitude increase with T. These evolutions with T arise from the difference between coercive bounds (field value at which μ_F is perpendicular to the field) and switching fields (which are defined as fields values at which the μ_F direction jumps[39]). Indeed, at 0 K, H_c diverges from the switching field when $\varphi > 45°$, and falls gradually to zero, whereas the later increases to converge back to its highest value at $\varphi = 90°$. However, at a non-zero T, this divergence occurs at a higher angle, which explains the H_c increase when T approaches the blocking temperature.

Whereas the SW model is often considered as a good approximation, it does not reproduce the evolutions discussed above. This non-zero temperature behavior should be considered in temperature dependence magnetization reversal studies.

B. Size-distributed F particles

In order to reproduce magnetic reversal behavior of actual systems, a large population of particles with different sizes should be included. Indeed, previous experimental studies have shown that the distribution of F particle sizes plays a key role for the understanding of ferromagnetic nanoparticle behavior.[26,52–54]

In the following, a lognormal distribution of particle diameters is used with a mean diameter $< d >= 8.29$ nm and standard deviation $\sigma_{sd} = 2.99$ nm. It should be noted that previous studies have shown that lognormal distributions are often observed in experimental systems.[22,29,52,54,55] The nanoparticles are assumed to be all aligned along their easy axis.

Figure 8 (left axis, round red symbols) shows the normalized particle size distribution D in the range of (4 to 25) nm, for 100 discrete d values. Each diameter has a corresponding effective magnetic moment per particle $\mu_{eff} = \mu_F \times D$. The normalized effective moment μ_{eff}/μ_{sat} is also shown in Fig. 8 (right axis), with μ_{sat} defining the saturated moment of the particle assembly. It shows that diameters which drive the magnetic behavior of the whole particle population are not around the maximum of the particle distribution nor the particle mean size, but are a compromise between the number of particles at that diameter and the corresponding total magnetic moment. The key point here is the effective magnetic moment distribution shown in Fig. 8.

The process for calculating the reversal cycle of an assembly of size-distributed particles is then as follows: for each diameter among the 100 discrete values, a reversal cycle is calculated. Considering no inter-particle interaction, the total magnetic moment is determined by the summation of each particle's moment, weighted by the density distribution.

Figure 9 shows the obtained $H_c(T)$ evolution for the previously defined assembly of particles, including magnetization reversal loops for multiple T in an inset. As a comparison, the

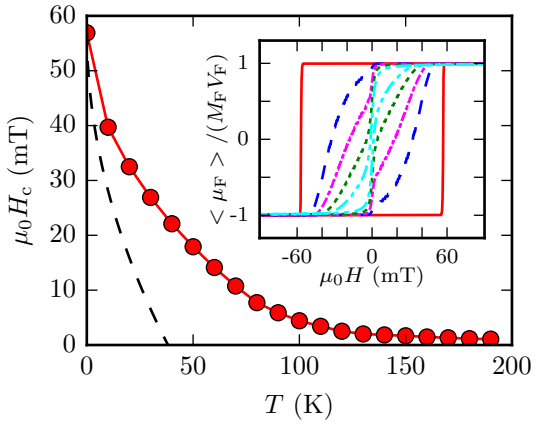

Figure 9. H_c temperature evolution (●) for a 100 discrete diameter size-distributed F nanoparticle assembly, and H_c evolution (– –) of a 8 nm single particle at $\varphi = 0°$ for comparison. The inset shows the corresponding reversal cycles for an assembly for $T =$ 0.01 K (——), 20 K (– –), 50 K (–·–·–), 100 K (····) and 190 K (–··–). $\varphi = 0°$ for all.

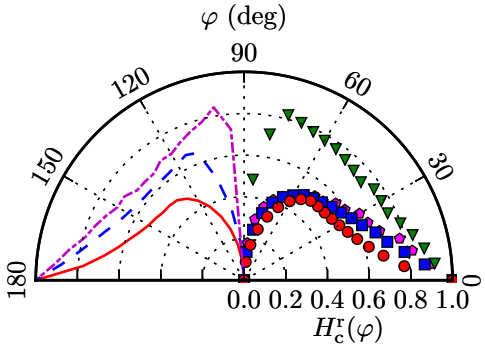

Figure 10. On the right quarter, azimuthal behavior of size-distributed particles for $T = 0.01$ K (●), 20 K (■), 50 K(⊠) and 100 K(▼). On the left quarter, for comparison, are plotted H_c^r for a 8 nm single particle for $T = 0.01$ K (——), 10 K (– –) and 30 K (–·–·–).

$H_c(T)$ evolution for a single particle (previously revealed in Fig. 6) is also shown. The critical temperature at which the coercivity is negligible for an assembly of particles (with a 8 nm average diameter) is much greater than for a 8 nm single diameter particle, as expected. The particle assembly exhibits a higher coercivity for non zero T due to the larger diameter population. It should be noted that, at $T = 0$ K, the coercive field for the assembly of particles is the same one than for a single particle. Indeed, all AF volumes are blocked at this temperature, and the free energy corresponds to the MB model providing a H_c value independent of F and AF volumes.

The thermal azimuthal behavior of size-distributed particles in Fig. 10 shows the same symmetry and shape as those obtained for a single particle in Fig. 7. Also, H_c^r are identical at 0 K. It should be noted that the evolution of the apex observed for a single particle is still present for a particle assembly.

IV. EXCHANGE BIASED NANOPARTICLES

This section focuses on core–shell exchange-coupled particles. The F core is now coupled to the AF shell with J_{eb}, K_{AF} and t_{AF} values from Tab. I. The fact that the AF domain is able to rotate is a driving mechanism for thermal dependence of magnetization reversal as explained below, and has only been simulated for thin film using a single domain[56,57] or multiple AF grains.[58]

Indeed, in a conventional MB model, the AF layer is rigid and cannot rotate. The exchange energy creates unbalanced energy valleys in the same way as a field strength would. Thus, the reversal cycle is field-shifted along the field axis, of a value H_e called the exchange-bias field. The thermal energy then only affects the switching field at which the reversal occurs. Hence, H_e does not depend on T and has a constant $J_{eb}S_{F/AF}$ value for $\varphi = 0°$.

However, when the AF spins are able to rotate, two additionnal energy valleys are available corresponding to the stable direction of the F spins with a reversed AF direction. The exchange coupling favors then the two opposite valleys where F and AF spins are parallels, as shown in Fig. 3. Depending on the ratio between the $\mathcal{F}$ energy terms, two different processes can be observed for a single F–AF particle. Below a temperature defined here as an exchange-blocking temperature where H_e is not zero, the AF shell anisotropy barrier is higher than the thermal fluctuation. The F moment rotates without dragging the AF, and a shift of the hysteresis cycle is observed. At a higher temperature, when the AF anisotropy energy barrier is low enough for the thermal fluctuation to be dominant, both F and AF rotate simultaneously, and no field shift is observed. Instead, as the effective anisotropy includes both F and AF anisotropies, the coercive field increases. The temperature at which the two behavior transitions occur depends directly on the AF anisotropy energy and exchange energy.

The two possible reversal mechanisms are shown in Figs. 11(a) and 11(b), representing the F and AF angle evolution with the applied field for the same parameters and at two different temperatures. For a high enough H, the F moment is dragged by H due to the Zeeman interaction, and the AF spin sublattice is dragged by the F moment due to the F–AF exchange interaction. At 0.01 K, only the F moment flips, and a shift is observed. The AF direction α also experiences a small hysteretic evolution, as shown in Fig. 11(a) for $\mu_0 H \in [-50, -25]$mT. At 15 K, all F and AF spins rotate simultaneously. The H_c bounds are then symmetrical, and no H_e exists. In-between these two different behaviors, H_e and H_c change abruptly due to the one-valley state approximation.

To create a particle size distribution, a F–AF core–shell particle size distribution is introduced through a F core log-normal distribution as described previously (see Fig. 8), with a constant AF shell thickness t_{AF}. The nanoparticles are as-

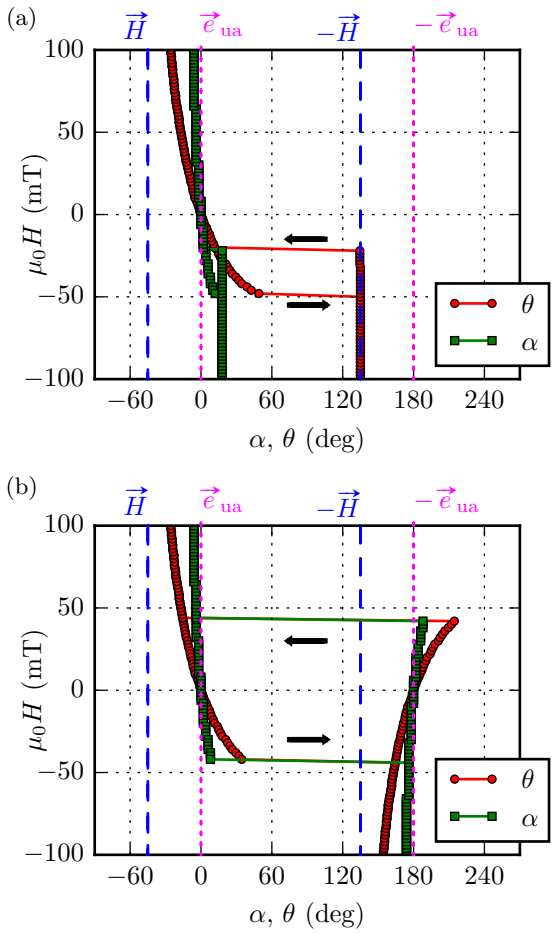

Figure 11. F and AF directions during a field cycle at $\varphi = 45°$, for (a) $T = 0.01\,\mathrm{K}$, and (b) $T = 15\,\mathrm{K}$. Obtained H_e values are $-33.7\,\mathrm{mT}$ and $0\,\mathrm{mT}$ respectively, and H_c values are $13.0\,\mathrm{mT}$ and $42.3\,\mathrm{mT}$. $\vec{H}$ (– –) and $\vec{e}_{ua}$ (····) represent the field and anisotropy axis directions, respectively.

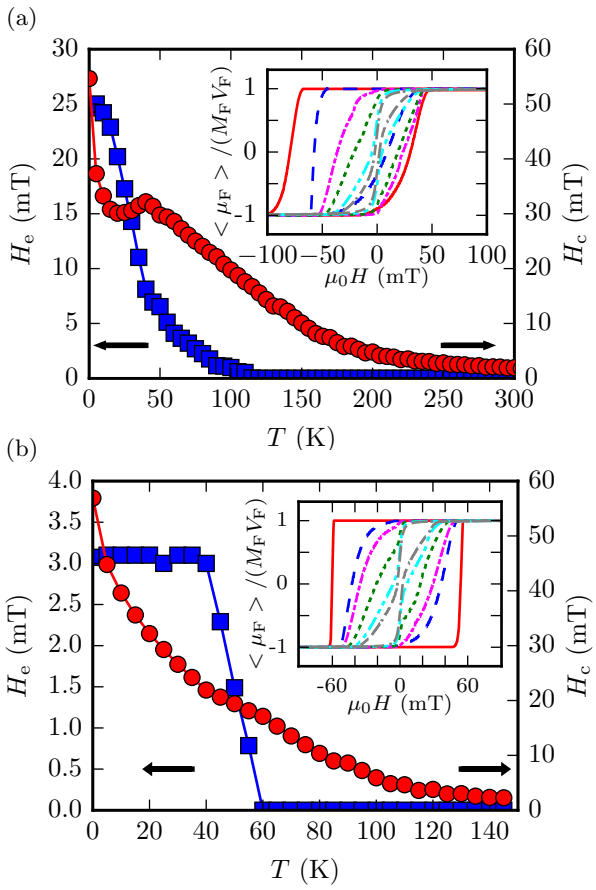

Figure 12. H_c (red circles) and H_e (blue squares) along the anisotropy axis for size-distributed F–AF core–shell particles. (a) corresponds to the (K_{AF}, J_{eb}) set of parameters. The inset shows corresponding reversal cycles for $T = 0.01\,\mathrm{K}$ (——), $10\,\mathrm{K}$ (– –), $50\,\mathrm{K}$ (-·-·), $100\,\mathrm{K}$ (····), $200\,\mathrm{K}$ (-··-) and $300\,\mathrm{K}$ (– ··). (b) shows H_c and H_e evolution for the (K^*_{AF}, J^*_{eb}) set, with the corresponding reversal cycles in the inset for $T = 0.01\,\mathrm{K}$ (——), $10\,\mathrm{K}$ (– –), $20\,\mathrm{K}$ (-·-·), $50\,\mathrm{K}$ (····), $100\,\mathrm{K}$ (-··-) and $145\,\mathrm{K}$ (– ··).

sumed to be all aligned along their easy axis.

The cycles obtained for different T are shown in Fig. 12(a) (inset), along with the temperature evolution of H_c (red circles, right axis) and H_e (blue squares, left axis).

The introduction of the F–AF exchange interaction in a size-distributed particle assembly results in an increase of the critical temperature at which H_c is negligible, as shown in Fig. 12(a). This coercive enhancement is an experimental phenomena previously observed in F–AF core–shell nanoparticles.[16,22] Here, this enhancement is clearly reproduced by the simulation for an assembly of F–AF particles and is due to the additional anisotropy of the rotating AF spins.

It should be noted that the F–AF exchange interaction results in a non-monotonic evolution of H_c with T. Indeed, a bump is present around 50 K as shown in Fig. 12(a). The H_c evolution is the result of the competition between the added AF anisotropy, and the thermal energy. A non-monotonic evolution of H_c has been previously experimentally observed in ferromagnetic-only nanoparticles,[59,60] and has been attributed to a frustrated magnetic surface state of the particles.[61] In our case, the surface state of the particles is an interfacial exchange interaction with an AF shell.

Additionally, a decrease of H_e with T is observed. Indeed, small particles exhibit a low exchange-blocking temperature, as this temperature depends on the anisotropy energy (related to the AF volume) and the interfacial exchange coupling energy (related to the F surface). Thus, the AF shell of small MNPs rotate with the F core, and induce an H_c enhancement. On the contrary, the AF shell of bigger MNPs stays frozen, and they do not participate in the H_c enhancement. Instead, they contribute to H_e. As the temperature increases, the blocked MNPs population decreases, and the exchange bias disappears.

The reversal cycles (inset in Fig. 12(a)) exhibit an asymmetry of magnetization reversal which evolves with T. This asymmetry is a specific property of exchange-biased systems,

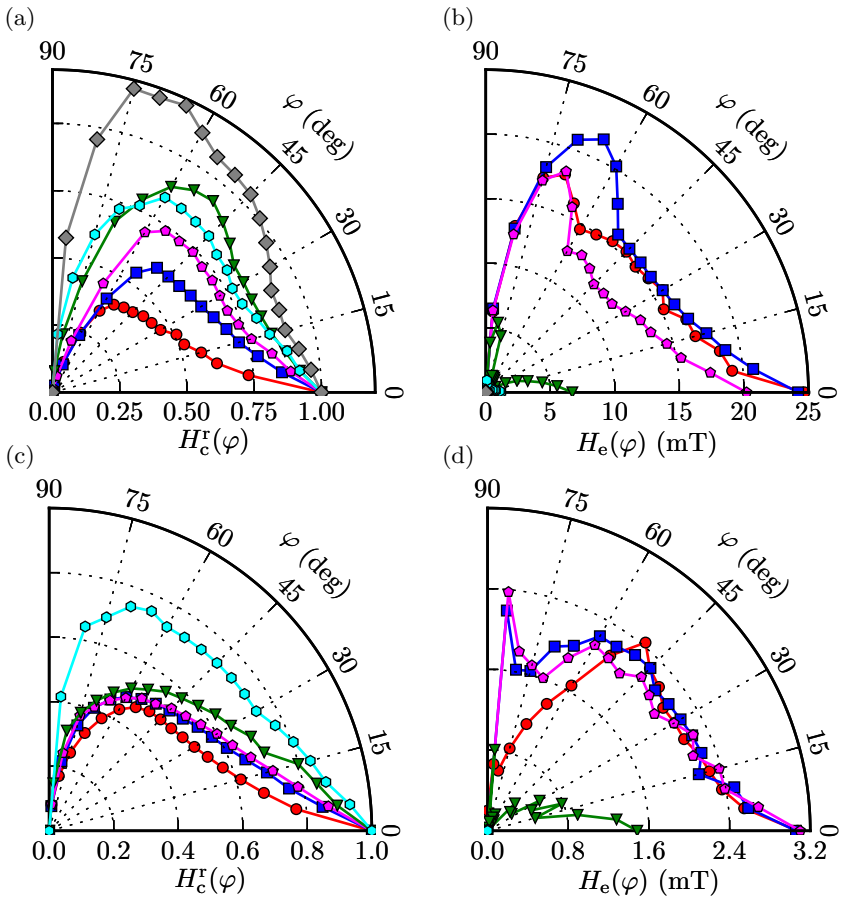

Figure 13. (a) H_c and (b) H_e angular thermal evolution of size-distributed core–shell particles with the (K_{AF},J_{eb}) set of parameters. (c) H_c and (d) H_e for the second set (K^*_{AF}, J^*_{eb}). Temperatures are $T = 0.01$ K (●), 10 K (■), 20 K (⊠), 50 K (▼), 100 K (⬟) and 200 K (◆).

as shown in previous studies.[62] Here, it is demonstrated that this asymmetry is also temperature dependent.

It is expected that H_c and H_e dependence on T evolves as a function of the F–AF properties (t_{AF}, K_F, K_{AF}, J_{eb}, etc.), even for particle systems with the same size distribution. To illustrate such a dependence, a second set of parameters (J^*_{eb} and K^*_{AF}) was used, defined in Tab. I. H_c and H_e dependence on T with this second set of parameters is shown in Fig. 12(b). A H_e saturation is observed below $T = 40$ K, and then H_e falls down to zero above. This H_e saturation is explained by the lower bound in the lognormal distribution, associated with a relatively small (J^*_{eb}, K^*_{AF}) compared to (J_{eb}, K_{AF}). Such a phenomenon was previously observed in an experimental study involving size-distributed Fe nanoparticles embedded in a Cr_2O_3 AF matrix.[29] The H_e maximum value is smaller than for the previous set of parameters (see Tab. I), as expected due to $J^*_{eb} < J_{eb}$. In addition, no exchange bias is observed for a low AF anisotropy, or a strong exchange coupling, that is, when $K_{AF}V_{AF} < J_{eb}S$. For a single 8 nm nanoparticle, the K_{AF} limiting value below which no exchange biased is observed is 133 kJ/m^3 for J_{eb}, and 18 kJ/m^3 for J^*_{eb}.

For H_c, a monotonic decrease is observed. It should be noted that the coercive enhancement (relative to F-only size-distributed MNPs) visible in Fig. 12(a) is no longer present. Moreover, the strong asymmetry observed in Fig. 12(a) (inset) is not visible anymore. Indeed, K^*_{AF} is much smaller than K_{AF}, as shown in Tab. I.

Finally, the H_c bump is observed for both sets of parameters, at $T = 40$ K in Fig. 12(a) and 60 K in Fig. 12(b). The amplitude and position of the bump are non-trivial, as these depend on the parameters of the system. Indeed, they are related to the apparition rate of the MNPs population with unblocked AF.

H_e and H_c angular dependence values for both sets of parameters are shown in Fig. 13. In both cases, shapes of H_c^r angular dependence with T are similar to the one observed previously in this paper. There are still apexes present in the figure, of which the angular position and amplitude evolve with T in a more complex manner. In particular, H_c^r values are greater than one in between $\varphi = 45°$ and 80° at 200 K for the (K_{AF}, J_{eb}) set of parameters, as shown in Fig. 13(a). Thus, this phenomena is only present for temperature close to the blocking temperature and for exchange biased MNPs. Also , it is not present for the other set of parameters and consequently depends on the ratio between the exchange bias en-

ergy and the AF anisotropy. It demonstrates that the complex summation of magnetization reversals within an assembly of particles leads to this remarkable phenomena of a H_c^r value greater than one. The model presented here reveals such a temperature dependent phenomena as it considers the magnetization reversal of each particle (including superparamagnetic and hysteretic behaviors).

The H_e angular dependence is strongly dependent on the (K_{AF}, J_{eb}) set of parameters, and also depends on T. The quantitative values obtained here are different than previously reported ones using similar models.[63,64] This is expected since a different energy function was considered in these previous studies, including additional term such as a cubic anisotropy term or a perpendicular coupling term, and it confirms that the exact form of the free energy is a driving mechanism for H_e and H_c values.

Consequently, probing the thermal dependence of H_e and H_c angular behaviors would contribute to a precise determination of magnetic constants in size-distributed core–shell nanoparticles.

V. CONCLUSION

In this paper, theoretical modeling of size-distributed F–AF core–shell nanoparticles is proposed, using F and AF uniaxial anisotropy. Thermal fluctuations were included with the Néel relaxation theory in a one-valley energy state approximation, by integrating over all the accessible states around the equilibrium valley. Also, for both sets of ferromagnetic-only particles and core–shell particles, a particle size distribution was introduced, assuming no inter-particle interactions, in order to reproduce actual systems.

This process made it possible to calculate temperature-dependent reversal behavior at different external field angles, for both F-only and F–AF exchange-coupled assembly of particles. The results obtained for a single F particle are in good agreement with previous models. In particular, ferromagnetic to superparamagnetic transition is obtained via multiple state integration. The exchange-coupled size-distributed particles show an additional anisotropy carried by the AF, increasing the overall blocking temperature. Increase of stability and coercive fields are important for applications such as magnetic storage or magnetic hyperthermia. Furthermore, this study shows that size-distributed exchange-coupled nanoparticles exhibit non-monotonic evolution of H_e and H_c with T. The angular dependence of H_c exhibits an apex, whose position and amplitude are strongly T-dependent. For exchange biased MNPs, it is shown that a reduced coercive field greater than one can be obtained. The angular dependence of H_e with T exhibits complex behaviors. Studying the thermal dependence of H_e and H_c angular behaviors would contribute to a precise determination of magnetic constants in size-distributed core–shell nanoparticles. These phenomena are beyond the scope of a non-temperature dependent model, such as the MB model. Whereas our model does include a size distribution, the development of models including inter-particle interactions and incoherent reversal modes in conjunction with a size-distributed assembly of nanoparticles would be of interest to progress beyond the model presented here.

In addition, no anisotropy dispersion are considered in this model. Such an absence of dispersion could be inferred by the cooling procedure in F–AF nanoparticles. However, the presence of anisotropy dispersion would modify the azimuthal behavior as well as the magnetization reversal of nanoparticle assemblies. Consequently, further theoretical modeling including such an effect would be of interest to complement the work presented here.

ACKNOWLEDGMENTS

This research was supported by the project 29785ZA in the programme Partenariat Hubert-Curien (PHC) and the France/SA NRF Protea grant (grant number 85059).

The program used for simulation is open-source software written in Python[65], using Scipy[66] and Matplotlib[67] libraries. The source code is freely available under the GPLv3 license on `https://github.com/LabMagUBO/StoneX` (doi: `http://dx.doi.org/10.5281/zenodo.58957`). In addition to the terms of the GPLv3, we kindly request that any work using this program refers to the latter website and this paper.

REFERENCES

[1] J. L. Dormann, D. Fiorani, and E. Tronc, "Magnetic relaxation in fine-particle systems," Advances in Chemical Physics Advances in Chemical Physics, **98**, 283–494 (1997).
[2] J. L. Dormann and D. Fiorani, *Magnetic Properties of Fine Particles* (Elsevier, 1992).
[3] O. Petracic, "Superparamagnetic nanoparticle ensembles," Superlattices and Microstructures **47**, 569–578 (2010).
[4] I. Obaidat, B. Issa, and Y. Haik, "Magnetic properties of magnetic nanoparticles for efficient hyperthermia," Nanomaterials **5**, 63–89 (2015).
[5] R. K. Gilchrist, R. Medal, W. D. Shorey, R. C. Hanselman, J. C. Parrott, and C. B. Taylor, "Selective inductive heating of lymph nodes." Annals of surgery **146**, 596–606 (1957).
[6] C. S. Kumar and F. Mohammad, "Magnetic nanomaterials for hyperthermia-based therapy and controlled drug delivery," Advanced Drug Delivery Reviews **63**, 789–808 (2011).
[7] B. Issa, I. M. Obaidat, B. A. Albiss, and Y. Haik, "Magnetic nanoparticles: surface effects and properties related to biomedicine applications." International journal of molecular sciences **14**, 21266–305 (2013).
[8] M. Bañobre-López, A. Teijeiro, and J. Rivas, "Magnetic nanoparticle-based hyperthermia for cancer treatment." Reports of practical oncology and radiotherapy : journal of Greatpoland Cancer Center in Poznań and Polish Society of Radiation Oncology **18**, 397–400 (2013).
[9] S. Dutz and R. Hergt, "Magnetic particle hyperthermia–a promising tumour therapy?" Nanotechnology **25**, 452001 (2014).
[10] J. Carrey, B. Mehdaoui, and M. Respaud, "Simple models for dynamic hysteresis loop calculations of magnetic single-domain nanoparticles: Application to magnetic hyperthermia optimization," Journal of Applied Physics **109**, 3921 (2011).
[11] D. Weller and A. Moser, "Thermal effect limits in ultrahigh-density magnetic recording," IEEE Transactions on Magnetics **35**, 4423–4439 (1999).
[12] R. Hergt, S. Dutz, R. Müller, and M. Zeisberger, "Magnetic particle hyperthermia: nanoparticle magnetism and materials development for cancer therapy," Journal of Physics: Condensed Matter **18**, S2919–S2934 (2006).
[13] G. Vallejo-Fernandez, O. Whear, A. G. Roca, S. Hussain, J. Timmis, V. Patel,

and K. O'Grady, "Mechanisms of hyperthermia in magnetic nanoparticles," Journal of Physics D: Applied Physics **46**, 312001 (2013).
[14]R. Rosensweig, "Heating magnetic fluid with alternating magnetic field," Journal of Magnetism and Magnetic Materials **252**, 370–374 (2002).
[15]H. Zhou and H. N. Bertram, "Effect of grain size distribution on recording performance in longitudinal thin film media," IEEE Transactions on Magnetics **36**, 61–66 (2000).
[16]R. F. L. Evans, R. Yanes, O. Mryasov, R. W. Chantrell, and O. Chubykalo-Fesenko, "On beating the superparamagnetic limit with exchange bias," EPL (Europhysics Letters) **88**, 57004 (2009).
[17]R. Hergt, S. Dutz, and M. Röder, "Effects of size distribution on hysteresis losses of magnetic nanoparticles for hyperthermia," Journal of Physics: Condensed Matter **20**, 385214 (2008).
[18]B. Mehdaoui, A. Meffre, J. Carrey, S. Lachaize, L.-M. Lacroix, M. Gougeon, B. Chaudret, and M. Respaud, "Optimal size of nanoparticles for magnetic hyperthermia: A combined theoretical and experimental study," Advanced Functional Materials **21**, 4573–4581 (2011).
[19]J.-H. Lee, J.-T. Jang, J.-S. Choi, S. H. Moon, S.-H. Noh, J.-W. Kim, J.-G. Kim, I.-S. Kim, K. I. Park, and J. Cheon, "Exchange-coupled magnetic nanoparticles for efficient heat induction." Nature nanotechnology **6**, 418–22 (2011).
[20]A. Moser, K. Takano, D. T. Margulies, M. Albrecht, Y. Sonobe, Y. Ikeda, S. Sun, and E. E. Fullerton, "Topical review: Magnetic recording: advancing into the future," Journal of Physics D: Applied Physics **35**, R157–R167 (2002).
[21]J. Nogués, V. Skumryev, J. Sort, S. Stoyanov, and D. Givord, "Shell-driven magnetic stability in core-shell nanoparticles," Physical Review Letters **97**, 157203 (2006).
[22]V. Skumryev, S. Stoyanov, Y. Zhang, G. Hadjipanayis, D. Givord, and J. Nogués, "Beating the superparamagnetic limit with exchange bias," Nature **423**, 850–853 (2003).
[23]H. F. Du and A. Du, "The hysteresis curves of nanoparticles obtained by monte carlo method based on the stoner-wohlfarth model," Journal of Applied Physics **99**, 104306 (2006).
[24]O. Iglesias, X. Batlle, and A. Labarta, "Microscopic origin of exchange bias in core/shell nanoparticles," Physical Review B **72** (2005), 10.1103/PhysRevB.72.212401.
[25]W. H. Meiklejohn and C. P. Bean, "New magnetic anisotropy," Physical Review **102**, 1413–1414 (1956); "New magnetic anisotropy," Physical Review **105**, 904–913 (1957).
[26]T. Jonsson, J. Mattsson, P. Nordblad, and P. Svedlindh, "Energy barrier distribution of a noninteracting nano-sized magnetic particle system," Journal of Magnetism and Magnetic Materials **168**, 269–277 (1997).
[27]B. Craig, R. Lamberton, A. Johnston, U. Nowak, R. W. Chantrell, and K. O'Grady, "A model of the temperature dependence of exchange bias in coupled ferromagnetic/antiferromagnetic bilayers," Journal of Applied Physics **103**, 07C102 (2008).
[28]C. Kittel, *Introduction to Solid State Physics, 8th ed.* (John Wiley & Sons, Inc., New York, 2005) p. 680.
[29]J. Sort, V. Langlais, S. Doppiu, B. Dieny, S. Suriñach, J. S. Muñoz, M. D. Baró, C. Laurent, and J. Nogués, "Exchange bias effects in Fe nanoparticles embedded in an antiferromagnetic Cr2O3 matrix," Nanotechnology **15**, S211–S214 (2004).
[30]G. F. Goya, S. Gómez, and S. Shibli, "Magnetic dynamics of iron-oxide nanoparticles in frozen ferrofluids and ferronematics," Journal of Metastable and Nanocrystalline Materials **22**, 33–38 (2004).
[31]B. Ruette, S. Zvyagin, A. P. Pyatakov, A. Bush, J. F. Li, V. I. Belotelov, A. K. Zvezdin, and D. Viehland, "Magnetic-field-induced phase transition in bifeo3 observed by high-field electron spin resonance: Cycloidal to homogeneous spin order," Physical Review B **69**, 064114 (2004).
[32]G. Vallejo-Fernandez, L. E. Fernandez-Outon, and K. O'Grady, "Measurement of the anisotropy constant of antiferromagnets in metallic polycrystalline exchange biased systems," Applied Physics Letters **91**, 212503 (2007).
[33]J. Nogués and I. K. Schuller, "Exchange bias," Journal of Magnetism and Magnetic Materials **192**, 203–232 (1999).
[34]O. Iglesias, X. Batlle, and A. Labarta, "Modelling exchange bias in core/shell nanoparticles," Journal of Physics: Condensed Matter **19**, 406232 (2007).
[35]L. Néel, "Théorie du trainage magnétique des ferromagnétiques au grains fin avec applications aux terres cuites," Annales de Geophysique **5**, 99–136 (1949).
[36]W. T. Coffey and Y. P. Kalmykov, "Thermal fluctuations of magnetic nanoparticles: Fifty years after brown," Journal of Applied Physics **112**, 121301 (2012).
[37]C. P. Bean and J. D. Livingston, "Superparamagnetism," Journal of Applied Physics **30**, S120 (1959).
[38]W. C. Nunes, W. S. D. Folly, J. P. Sinnecker, and M. A. Novak, "Temperature dependence of the coercive field in single-domain particle systems," Physical Review B **70**, 014419 (2004).
[39]J. García-Otero, A. J. García-Bastida, and J. Rivas, "Influence of temperature on the coercive field of non-interacting fine magnetic particles," Journal of Magnetism and Magnetic Materials **189**, 377–383 (1998).
[40]J. García-Otero, M. Porto, J. Rivas, and A. Bunde, "Influence of the cubic anisotropy constants on the hysteresis loops of single-domain particles: A monte carlo study," Journal of Applied Physics **85**, 2287 (1999).
[41]V. Franco and A. Conde, "Thermal effects in a stoner–wohlfarth model and their influence on magnetic anisotropy determination," Journal of Magnetism and Magnetic Materials **278**, 28–38 (2004).
[42]H. Pfeiffer, "Relaxation behaviour of magnetic particle assemblies due to thermal fluctuations," physica status solidi (a) **120**, 233–245 (1990).
[43]H. Pfeiffer, "Influence of thermal fluctuations on the magnetic properties of particle assemblies," physica status solidi (a) **122**, 377–389 (1990).
[44]O. Iglesias and A. Labarta, "Magnetic field scaling of relaxation curves in small particle systems," Journal of Applied Physics **91**, 4409 (2002).
[45]C. Xu, Z. Y. Li, and P. M. Hui, "Monte carlo studies of hysteresis curves in magnetic composites with fine magnetic particles," Journal of Applied Physics **89**, 3403 (2001).
[46]T. Ambrose, R. L. Sommer, and C. L. Chien, "Angular dependence of exchange coupling in ferromagnet/antiferromagnet bilayers," Physical Review B **56**, 83–86 (1997).
[47]J.-V. Kim, R. L. Stamps, B. V. McGrath, and R. E. Camley, "Angular dependence and interfacial roughness in exchange-biased ferromagnetic/antiferromagnetic bilayers," Physical Review B (Condensed Matter and Materials Physics) **61**, 8888–8894 (2000).
[48]E. Jiménez, J. Camarero, P. Perna, N. Mikuszeit, F. J. Terán, J. Sort, J. Nogués, J. M. García-Martín, A. Hoffmann, B. Dieny, and R. Miranda, "Role of anisotropy configuration in exchange-biased systems," Journal of Applied Physics **109**, 07D730 (2011).
[49]W. Zhang, D. N. Weiss, and K. M. Krishnan, "Competing anisotropies and temperature dependence of exchange bias in co/irmn metallic wire arrays fabricated by nanoimprint lithography," Journal of Applied Physics **107**, 09D724 (2010).
[50]D. T. Dekadjevi, T. Jaouen, D. Spenato, S. P. Pogossian, and J. Ben Youssef, "Experimental evidences and driving mechanisms for anisotropic misalignments in exchange coupled systems," The European Physical Journal B **80**, 121–125 (2011).
[51]E. C. Stoner and E. P. Wohlfarth, "A mechanism of magnetic hysteresis in heterogeneous alloys," Philosophical Transactions of the Royal Society A: Mathematical, Physical and Engineering Sciences **240**, 599–642 (1948).
[52]S. Tiwari and K. Rajeev, "Effect of distributed particle magnetic moments on the magnetization of nio nanoparticles," Solid State Communications **152**, 1080–1083 (2012).
[53]L. Khanna and N. Verma, "Size-dependent magnetic properties of calcium ferrite nanoparticles," Journal of Magnetism and Magnetic Materials **336**, 1–7 (2013).
[54]K. Pisane, E. Despeaux, and M. Seehra, "Magnetic relaxation and correlating effective magnetic moment with particle size distribution in maghemite nanoparticles," Journal of Magnetism and Magnetic Materials **384**, 148–154 (2015).
[55]K. Nishioka, C. Hou, H. Fujiwara, and R. D. Metzger, "Grain size effect on ferro-antiferromagnetic coupling of nife/femn systems," Journal of Applied Physics **80**, 4528 (1996).
[56]C. Binek, A. Hochstrat, and W. Kleemann, "Exchange bias in a generalized meiklejohn-bean approach," Journal of Magnetism and Magnetic Materials **234**, 353–358 (2001).
[57]D. Lebeugle, A. Mougin, M. Viret, D. Colson, J. Allibe, H. Béa, E. Jacquet, C. Deranlot, M. Bibes, and A. Barthélémy, "Exchange coupling with the multiferroic compound $bifeo_3$ in antiferromagnetic multidomain films and single-domain crystals," Physical Review B **81**, 134411 (2010).
[58]C. Hou, H. Fujiwara, K. Zhang, A. Tanaka, and Y. Shimizu, "Tempera-

ture dependence of the exchange-bias field of ferromagnetic layers coupled with antiferromagnetic layers," Physical Review B **63**, 024411 (2000).
[59]R. Zysler, H. Romero, C. Ramos, E. Biasi, and D. Fiorani, "Evidence of large surface effects in co–ni–b amorphous nanoparticles," Journal of Magnetism and Magnetic Materials **266**, 233–242 (2003).
[60]B. N. Pianciola, E. Lima, H. E. Troiani, L. C. Nagamine, R. Cohen, and R. D. Zysler, "Size and surface effects in the magnetic order of cofe2o4 nanoparticles," Journal of Magnetism and Magnetic Materials **377**, 44–51 (2015).
[61]E. De Biasi, C. Ramos, R. Zysler, and D. Fiorani, "Metropolis algorithm for simulating hysteresis in ferromagnetic nanoparticles," Physica B: Condensed Matter **372**, 345–349 (2006).
[62]D. Spenato, S. P. Pogossian, and H. Le Gall, "Asymmetric magnetization reversal in exchange-biased polycrystalline f/af bilayers," Journal of Magnetism and Magnetic Materials **262**, 294–301 (2003).
[63]P. Blomqvist and K. M. Krishnan, "Exchange coupling in nanoscale mnpd/fe heterostructures," Journal of Magnetism and Magnetic Materials **272**, 1237–1239 (2004).
[64]D. Givord, V. Skumryev, and J. Nogués, "Exchange coupling mechanism for magnetization reversal and thermal stability of co nanoparticles embedded in a coo matrix," Journal of Magnetism and Magnetic Materials **294**, 111–116 (2005).
[65]T. E. Oliphant, "Python for scientific computing," Computing in Science & Engineering **9**, 10–20 (2007).
[66]S. V. D. Walt, S. C. Colbert, and G. Varoquaux, "The numpy array: a structure for efficient numerical computation," Computing in Science and Engineering 13, 2 (2011) 22-30 (2011), 10.1109/MCSE.2011.37.
[67]J. D. Hunter, "Matplotlib: A 2d graphics environment," Computing in Science & Engineering **9**, 90–95 (2007).